Two-Dimensional Layered Hydroxide Nanoporous Nanohybrids Pillared with Zero-Dimensional Polyoxovanadate Nanoclusters for Enhanced Water Oxidation Catalysis

Jayavant L. Gunjakar,[a,b] Bo Hou,[c] Akbar I. Inamdar,[a] S. M. Pawar,[a] Abu Talha Aqueel Ahmed,[a] Harish S. Chavan, [a] Jongmin Kim,[a] Sangeun Cho,[a] Yongcheol Jo,[a] Seong-Ju Hwang,[d] SeungNam Cha,[c] Hyungsang Kim[a,*] and Hyunsik Im[a,*]

[a] *Division of Physics and Semiconductor Science, Dongguk University, Seoul 04620, South Korea*

[b] *D. Y. Patil Education society (Deemed to be University), Kolhapur, MS, India 416006*

[c] *Department of Engineering Science, University of Oxford, Parks Road, OX1 3PJ, UK*

[d] *Center for Intelligent Nano-Bio Materials (CINBM), Department of Chemistry and Nano Sciences, Ewha Womans University, Seoul 03670, Korea*

* Corresponding authors: hskim@dongguk.edu and hyunsik7@dongguk.edu

Keywords: Layered nickel hydroxide, nanocluster intercalation, water oxidation catalysis, chemical solution growth, controlled nanoporosity

Abstract

The oxygen evolution reaction (OER) is critical in electrochemical water splitting and requires an efficient, sustainable and cheap catalyst for successful practical applications. A common development strategy for OER catalysts is to search for facile routes for the synthesis of new catalytic materials with optimized chemical compositions and structures. Here, we report nickel hydroxide $Ni(OH)_2$ two-dimensional (2D) nanosheets pillared with zero-dimensional (0D) polyoxovanadate (POV) nanoclusters as an OER catalyst that can

operate in alkaline media. The intercalation of POV nanoclusters into $Ni(OH)_2$ induces the formation of a nanoporous layer-by-layer stacking architecture of 2D $Ni(OH)_2$ nanosheets and 0D POV with a tunable chemical composition. Our nanohybrid catalysts remarkably enhance the OER activity of pristine $Ni(OH)_2$. The present findings demonstrate that the intercalation of 0D POV nanoclusters into $Ni(OH)_2$ is effective for improving water oxidation catalysis and represents a potential method to synthesize novel, porous hydroxide-based nanohybrid materials with superior electrochemical activities.

Introduction

The electrocatalytic generation of H_2 and O_2 molecules via the electrolysis of water molecules is the focus of a great amount of research activity because of its usefulness for harnessing intermittent energy from the sun, wind, or other renewable sources and transforming the energy into user-friendly chemical energy.[1–4] The total water splitting reaction is composed of oxygen- and hydrogen-evolution half-reactions at the cathode ($2\ H^+(aq) + 2e^- \rightarrow H_2(g)$) and the anode ($2\ H_2O(l) \rightarrow O_2(g) + 4\ H^+(aq) + 4e^-$), respectively.[5] Despite its advantages, the electrolysis of water requires a substantial overpotential (η) in addition to the thermodynamic potential for water splitting ($H_2O \rightarrow H_2 + 0.5O_2$, 1.23 V), which is primarily the reason for the sluggish oxygen evolution reaction (OER) kinetics.[5,6] An electrocatalyst assists in the transfer of charge carriers between the electrode and the reactants or facilitates an intermediate chemical transformation that is described by an overall half-reaction, and noble metal (Rh/Ru/Ir) oxides are the most efficient and robust OER catalysts in acidic and alkaline media.[6,7] However, the high cost and relative scarcity of noble metal oxides restrict their practical applications.

The continued exploration of efficient, earth-abundant OER catalysts has led to the establishment of several new, earth-abundant OER catalysts that are based on transition-metal compounds such as oxides, layered double hydroxide (LDH), chalcogenides and carbon with catalytic activities that are comparable to those of IrO_2 and RuO_2.[6–9] However, most of the existing OER catalysts that have been developed do not possess a sufficiently high efficiency and stability for the electrocatalytic OER activity because of their non-optimized intrinsic properties, such as their electroconductivity, binding energy to the OER intermediate, and chemical composition, as well as their extrinsic properties, such as the particle size, morphology, and porosity. One of the most effective methods to tailor the intrinsic properties of catalytic materials

is to control their chemical composition. The ability to easily tailor their electronic structure via doping has made layered hydroxides promising electrocatalytic OER candidates in basic media.

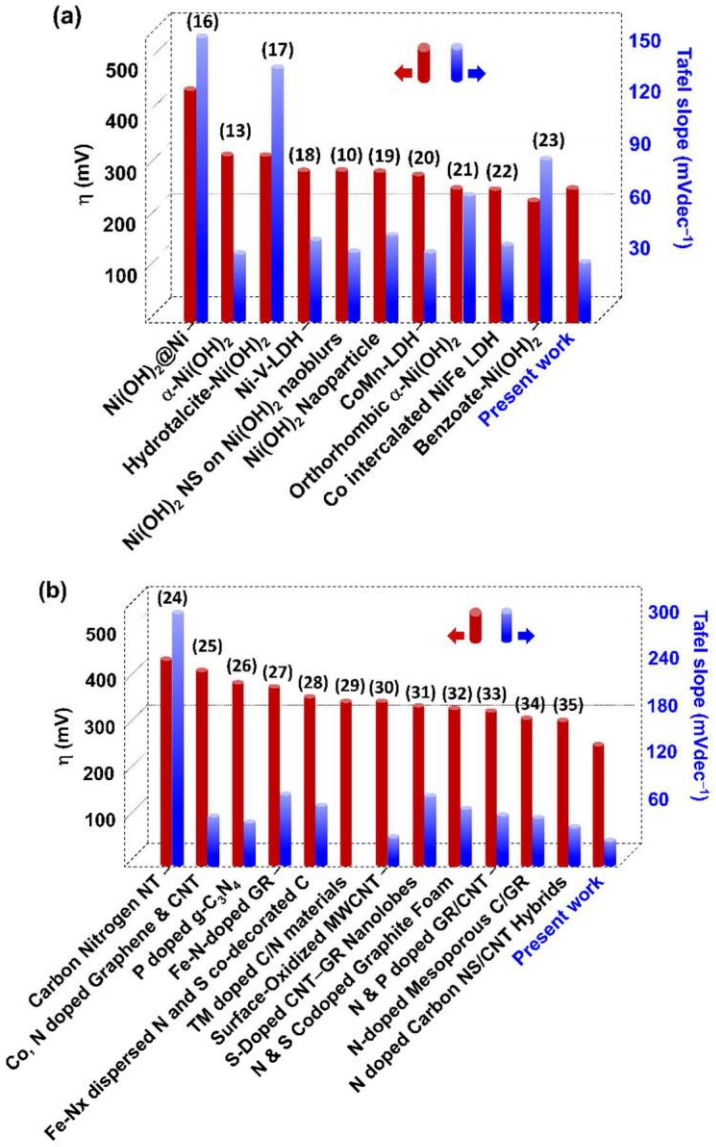

Fig. 1. The comparative literature survey: Overpotential (η) and Tafel slope for (a) $Ni(OH)_2$ and (b) carbon based OER electrocatalysts. Reference numbers are placed in parentheses.

Recently, nickel (Ni)-based double hydroxide compounds have attracted attention due to their high abundance, low cost, and superior electrocatalytic OER activities in alkaline media.[10–13] Among numerous nanostructured Ni-based layered hydroxides, Ni hydroxide ($Ni(OH)_2$) incorporated with metal elements has been the most intensively investigated as an electrocatalytic material because of its low overpotential and high electrolysis current.[12,14,15] Reported overpotential and Tafel slope values of various nanostructured nickel hydroxide and carbon based OER electrocatalysts are summarized in Figure 1.[10,13,16-35]

In addition to tuning the chemical composition, the hybridization of $Ni(OH)_2$, e.g., as nanoparticles, carbon nanotubes, and graphene nanosheets, is also equally effective for optimizing the OER activity because it results in improved electronic conductivity, high absorptivity of target molecules, high porosity, large surface area, and improved morphology. Because the α-$Ni(OH)_2.xH_2O$ polymorph consists of hydroxyl-deficient layers of β-$Ni(OH)_2$ and is oriented parallel to the crystallographic ab plane, it can act as an effective host lattice for the intercalation of numerous anionic guest species.[36] The well-defined molecular size, negative charge, and excellent redox properties of 0D polyoxometalate (POM) nanoclusters make them useful guest species for the hybridization of Ni-based layered hydroxides.[37] The intercalation of 0D POM in a layered hydroxide lattice with well-defined dimensions and cluster charges enables effective physical contact and a porous stacking structure with a large number of active catalytic sites.[38,39] In addition, the limited accessibility of the interlayer gallery space of the LDH that precludes the practical application of this material can be improved by the intercalation of POM nanoclusters.[40] Although several types of hybrids with Ni hydroxide and low-dimensional nanostructured materials have been studied, the direct synthesis of a hybrid OER electrocatalyst that is composed of 0D POM intercalated $Ni(OH)_2$ has been rarely reported.

In the present work, mesoporous layer-by-layer-ordered $Ni(OH)_2$-based nanohybrids intercalated with 0D polyoxovanadate (POV) nanoclusters are synthesized using a bottom-up chemical solution growth (CSG) method (the intercalative nanohybrids are denoted "NHV"). The effects of the POV-intercalative hybridization on the electrocatalytic OER activity and the surface area of the pristine $Ni(OH)_2$ material are investigated with the accompanying variations in the crystal structures and physicochemical properties.

Results and discussion

Fabrication of LDHs intercalated with 0D polyoxovanadate nanoclusters.

To investigate the effect of the POV intercalation on the physicochemical properties of the resulting NHV-nanohybrid materials, four representative $Ni(OH)_2$/POV molar ratios were selected. The $Ni(OH)_2$/POV molar ratios of 6.66, 2, 1, and ∞ were selected, and the obtained nanohybrids are denoted NHV-1.5, NHV-5, NHV-10, and NHV-∞, respectively. The $Ni(OH)_2$/POV molar ratios of 6.66, 2, and 1 correspond to 1.5-, 5-, and 10-fold excesses of POV, respectively, which were estimated based on the lower-nuclearity $[V_2O_7]^{4-}$ POV nanoclusters. The NHV-∞ sample represents the pristine $Ni(OH)_2$ sample.

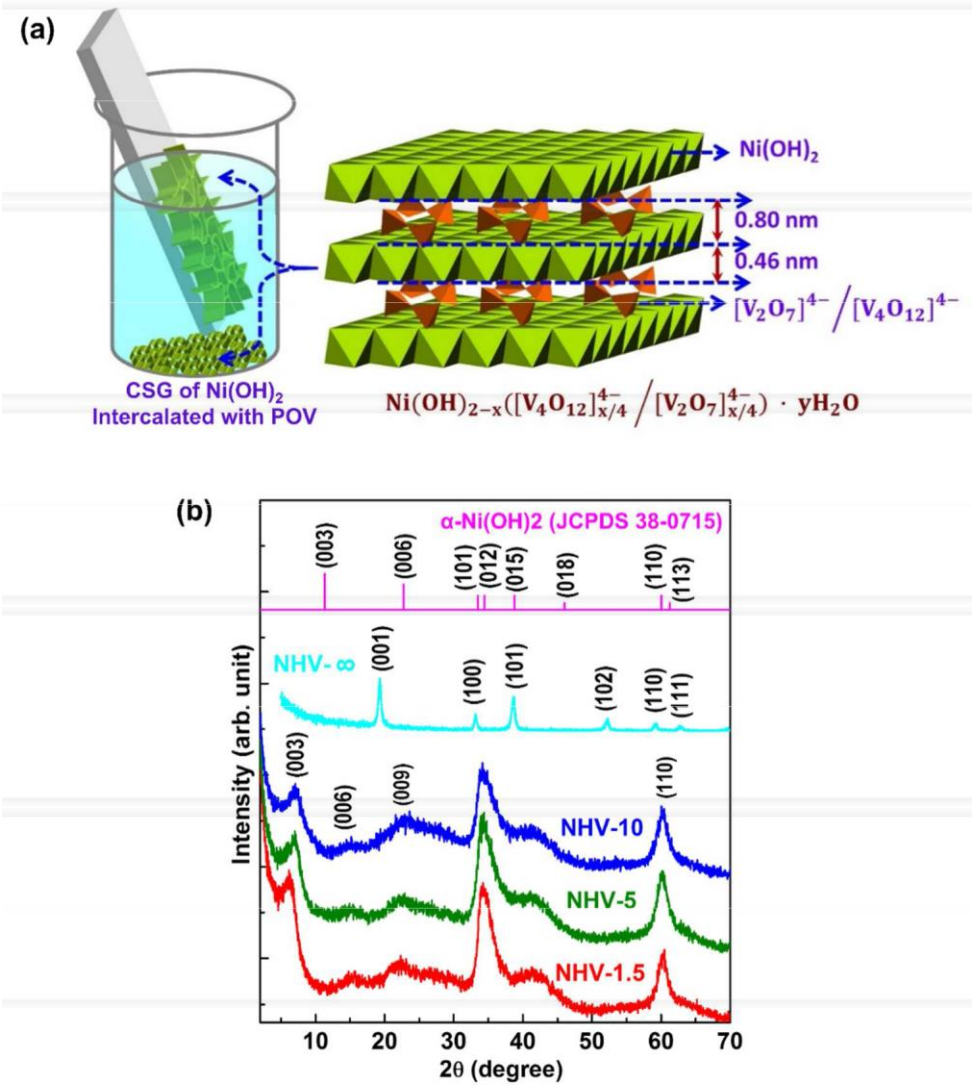

Fig. 2. Schematic illustration of the synthesis and structural characterization of the nanohybrids. (a) Schematic structure model of the NHV nanohybrids. (b) X-ray diffraction (XRD) patterns of the nanohybrids: (red) NHV-1.5, (green) NHV-5, (blue) NHV-10, (cyan) NHV-∞, and (pink) α-$Ni(OH)_2$ (JCPDS 38-0715).

The crystal structures of the NHV nanohybrids were examined using powder X-ray diffraction (XRD) analyses. The powder XRD patterns of the NHV nanohybrids are presented in

Figure 2 with those of the pristine β-$Ni(OH)_2$ (NHV-∞) and α-$Ni(OH)_2$ (JCPDS 38-0715). The pristine NHV-∞ sample shows several Bragg reflections with a highly intense (001) reflection, which correspond to the β-$Ni(OH)_2$ structure. According to the least-squares fitting analysis, the lattice parameters *a* and *c* of the NHV-∞ sample are 0.31 nm and 0.46 nm, respectively, which are in good agreement with those of β-$Ni(OH)_2$. Alternatively, a series of equally spaced (*00l*) Bragg reflections are commonly observed for all of the NHV nanohybrids in the low 2θ region, and the shifting of the (*00l*) Bragg reflections to a low 2θ value clearly indicates the formation of a layer-by-layer, ordered intercalative structure composed of interstratified $Ni(OH)_2$ and 0D POV nanoclusters. Regardless of the $Ni(OH)_2$-POV ratio, all of the NHV nanohybrids demonstrate the formation of a layer-by-layer, ordered structure with expanded basal spacings of 1.2-1.4 nm. This result indicates that the intercalation of the POV nanoclusters in the gallery space of the $Ni(OH)_2$ is highly flexible regarding the chemical composition of the hybrid materials. Among the nanohybrids, NHV-1.5, which has the lowest POV content, shows the largest gallery height of 1.4 nm. The highest basal spacing at a 1.5-fold POV excess clearly indicates the intercalation of a high-nuclearity, cyclic metavanadate $[V_4O_{12}]^{4-}$ species. The observed intercalation of the $[V_4O_{12}]^{4-}$ species is attributed to the stabilization of a pH of ~ 8 during the growth of the NHV-1.5 nanohybrid. Meanwhile, for the 5 and 10-fold excesses of POV, the NHV nanohybrids have basal spacings of 1.25 nm and 1.29 nm, respectively. The observed basal spacings clearly suggest the intercalation of a low-nuclearity, dimeric pyrovanadate $[V_2O_7]^{4-}$ species due to the stabilization of a high pH (~10) during the growth of the NHV-5 and NHV-10 nanohybrids. For the $Ni(OH)_2$-POV ratios above 10 and below 1.5, a well-ordered, layer-by-layer intercalated structure does not form. Based on the Scherrer calculation at the full-width-at-half-maximum (FWHM) of the (*00l*) reflections, the estimated thickness of each crystallite along the *c*-axis is ~

60~90 Å. Based on the basal spacings of the NHV nanohybrids, the crystallite thickness corresponds to ~ 5−7 $Ni(OH)_2$ monolayers that are pillared with POV. As can be seen clearly from Figure 2, all of the NHV nanohybrids display the characteristic in-plane (*110*) peak of hexagonal $Ni(OH)_2$ sheets at 2θ = ~ 60.2° and a broad hump peak at ~ 32−45°, highlighting the growth of the $Ni(OH)_2$ in-plane structure with a turbostratic structure.[41]

Reaction Mechanism.

The CSG of thin films is a controlled precipitation technique that is based on the principle of solid phase formation during the transformation from a supersaturated state to a saturated state.[42] For the synthesis of the $Ni(OH)_2$−POV nanosheet thin films, a supersaturated aqueous solution of a hexamine $Ni(NH_3)_4^{+2}$ complex and sodium orthovanadate (Na_3VO_4) transforms into a saturated state via the gradual evaporation of ammonia (NH_3). The CSG bath is maintained at a constant temperature of 50 ºC. The dissolution of $NiCl_2$ in water initially facilitates the emergence of an octahedral hexa-aqua nickel (II) complex ion, as follows:[43]

$$xNiCl_2 + xyH_2O \rightarrow x[Ni(H_2O)_y]^{2+}_{(aq)} + 2x(Cl_2)^- \quad (1)$$

During the addition of the liquid NH_3, a greenish precipitate of the hydrated $Ni(OH)_2$ forms via the hydroxide group-derived *olation* process of the stepwise replacement of the H_2O ligand molecules, as follows:

$$\begin{aligned} x[Ni(H_2O)_p]^{2+} + y(OH)^{2-} &\leftrightarrow [Ni_x(OH)_y(H_2O)_{xp-y}]^{(2x-y)+} \text{at pH} < 9, \\ x[Ni(H_2O)_p]^{2+} + y(OH)^{2-} &\leftrightarrow Ni_x(OH)_{2n}(s) + (xp-y)H^+ \text{at pH} > 9 \end{aligned} \quad (2)$$

Upon the further addition of excess NH_3, the $Ni(OH)_2$ green precipitate transforms into a clear blue solution of the hexamine nickel complex ($Ni(NH_3)_q^{2+}$), where q is the coordination number, and 6 is the most stable for Ni^{2+}.[44,45] The formation of the hexamine nickel complex prevents a spontaneous precipitation, leading to the formation of a supersaturated solution, as follows:

$$Ni_x(OH)_{2x} + qNH_4^+ + q(OH)^- \rightarrow Ni_x(NH_3)_q^{2x+} + qH_2O + 2x(OH)^- \text{ at pH} > 12 \quad (3)$$

The aqueous solution of the vanadium precursor produces a large variety of POV species with diverse structures, e.g., chain metavanadates $[VO_3^-]_n$, layered oxides $[V_2O_5]$, and compact polyanions $[V_{10}O_{28}]^{6-}$. The structural nature of these species is highly dependent on the concentration and pH.[43,46,47] The V^{5+} ions induce the $[V(OH_2)_6]^{5+}$ solvated species that are formed in aqueous solution and are surrounded by dipolar H_2O molecules.

Because V^{5+} and H_2O possess a strong polarizing power and Lewis properties, respectively, some of the electrons transfer from the $3a_1$ orbital of the water molecule to the empty 3d orbitals in the V^{5+}. The resultant spontaneous acidification and deprotonation of the H_2O molecules are represented by the following hydrolysis reaction:

$$[V(OH_2)_6]^{5+} + hH_2O \rightarrow [V(OH)_h(OH_2)_{6-h}]^{(5-h)+} + hH_3O^+ \quad (4)$$

where the hydrolysis ratio, *h*, increases with the pH, leading to the formation of aquo, hydroxo, or oxo species. Initially, the pH of the Na_3VO_4 solution is close to ~ 12, and the monomeric, tetrahedralvanadate oxo-anionic VO_4^{3-} species is produced. The vanadium in the solution is surrounded by four equivalent oxygen atoms. A $Ni(OH)_2$–POV CSG bath is produced via the

addition of a monomeric orthovanadate (VO_4^{3-}) solution to the supersaturated hexamine nickel complex solution. The addition of this solution leads to a transparent, supersaturated CSG bath with a slight increase in the pH depending on the amount of the VO_4^{3-} precursor, and the colour changes from transparent blue to dark cyan. The CSG bath is maintained at an elevated temperature (~50 ºC) with the vertically immersed substrates. Consequently, the ionic product exceeds its solubility product via the release of H_2O and NH_3. The CSG bath gradually becomes saturated, and precipitation occurs through the heterogeneous growth of $Ni(OH)_2$ that has been pillared with the POV species on the substrate and homogeneous growth in the solution phase.

The type of the intercalated species can be predicted by observing the change in the pH. As the precipitation process proceeds, the pH changes from 12.5 to ~ 7. As the pH gradually decreases to ~9, condensation occurs due to the continuous deprotonation that leads to the transformation of the VO_4^{3-} species into dimeric pyrovanadates $[V_2O_7]^{4-}$. In the pH range from 7 to 9, more condensed, cyclic-metavanadate $[V_4O_{12}]^{4-}$can form.[46] Consequently, the intercalated POV species are most likely $[V_2O_7]^{4-}$ or $[V_4O_{12}]^{4-}$.

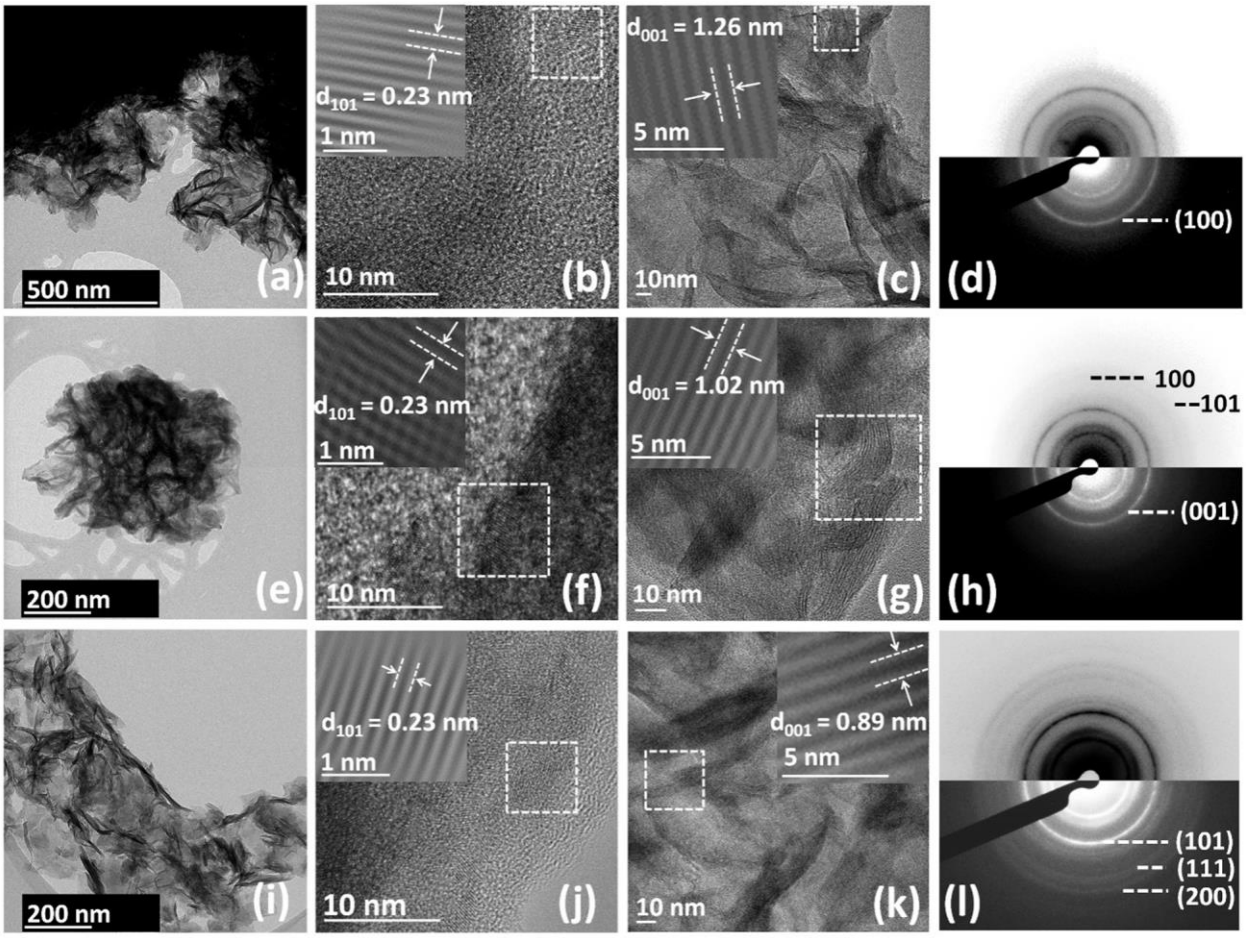

Fig. 3. High-resolution transmission electron microscopy analysis of the nanohybrids. High-resolution transmission electron microscopy (HR-TEM) images and selected area electron diffraction (SAED) patterns of the NHV nanohybrids: (a–d) NHV-1.5, (e–h) NHV-5, and (i–l) NHV-10. The insets show the lattice fringes.

Structural and surface morphological study.

The localized crystal shape and formation of the layer-by-layer intercalated structure of the $Ni(OH)_2$ and POV nanoclusters are confirmed by high-resolution transmission electron microscopy (HR-TEM) and selected area electron diffraction (SAED) analyses. Figure 3 clearly shows at a low magnification the interconnected, house-of-cards-type networks in the $Ni(OH)_2$-

layered crystallites that are intercalated with the POV nanoclusters for all of the NHV nanohybrids. As illustrated in the insets of Figure 3, at a high resolution, two types of parallel-aligned lines with different separation distances are resolved in the NHV nanohybrids. One type is in the plane view with a smaller spacing of 0.23 nm, and the other type is in the cross-sectional view with a larger spacing of ~ 0.9-1.2 nm. The observed interline distances from the top and cross-sectional views are in good agreement with the in-plane and *c*-axis lattice parameters that are determined from the XRD analysis. The present assignment is further probed using the SAED analysis, as shown in Figure 3(d,h,l). The SAED images clearly exhibit typical electron diffraction patterns for hexagonal $Ni(OH)_2$ nanosheets.[48] The sharp continuous diffraction rings readily index to the (100), (101), (111), (002), and (200) planes of the host $Ni(OH)_2$ lattice.[49,50] In addition to the sharp diffraction rings, several broad and diffuse rings are also detected, and these are attributed to the diffractions from the stabilization of the POV nanoclusters between the $Ni(OH)_2$ nanosheets. The present HR-TEM images of the NHV nanohybrids are analogous to those of nanohybrids synthesized using exfoliated metal-oxide/LDH 2D nanosheets and guest 0D nanoclusters via an exfoliation-restacking self-assembly route.[40,51]

The elemental distributions in the NHV nanohybrids are investigated using a scanning transmission electron microscope (STEM) equipped with an energy dispersive spectroscopy (EDS) detector. The elemental EDS line profiles of the NHV nanohybrids clearly demonstrate the homogeneous distribution of nickel, vanadium, and oxygen in the $Ni(OH)_2$-POV crystallites (**Supporting Fig. S1**).The STEM elemental mapping results also clearly confirm the intimate and homogeneous intercalation of the POV nanoclusters between the $Ni(OH)_2$ nanosheets.

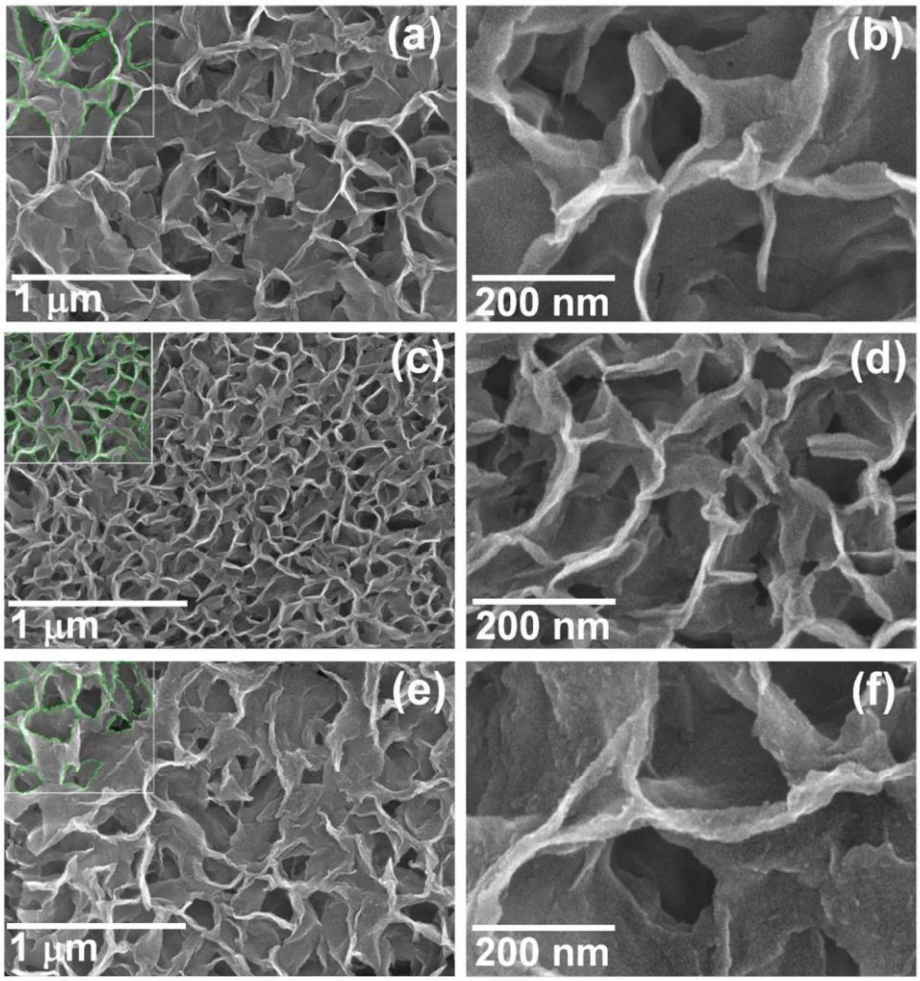

Fig. 4. Surface morphology of the nanohybrids. Field emission-scanning electron microscopy (FE-SEM) images of the nanohybrids: (a, b) NHV-1.5, (c, d) NHV-5, and (e, f) NHV-10.

The surface morphologies of the NHV nanohybrids are investigated using field emission-scanning electron microscopy (FE-SEM). As presented in Figure 4, all of the NHV nanohybrids exhibit nanosheets that have vertically grown on the substrate surface. Despite the different reaction conditions, the NHV nanohybrids show similar house-of-cards-type morphologies that areformed by the interconnection of the $Ni(OH)_2$-POV nanosheets. This type of nanosheet morphology is commonly observed for CSG-deposited hydroxide materials.[52] The estimated

nanosheet thicknesses of 5–15 nm corresponds to between 3 and 6 stacked layers of 2D $Ni(OH)_2$ with POV. The chemical compositions of the $Ni(OH)_2$–POV nanohybrids are quantitatively determined with EDS elemental mapping analyses. The EDS analysis clearly demonstrate the homogeneous distribution of Ni, V, and O over the $Ni(OH)_2$–POV nanohybrid crystallites. Based on the EDS elemental analysis the chemical compositions of the $Ni(OH)_2$–POV nanohybrids are estimated to be $Ni(OH)_{1.67}{\cdot}0.08(V_4O_{12})^{4-}{\cdot}yH_2O$, $Ni(OH)_{1.96}{\cdot}0.16(V_2O_7)^{4-}{\cdot}yH_2O$ and $Ni(OH)_{1.962}{\cdot}0.15(V_2O_7)^{4-}{\cdot}yH_2O$ for NHV-1.5, NHV-5, and NHV-10, respectively.

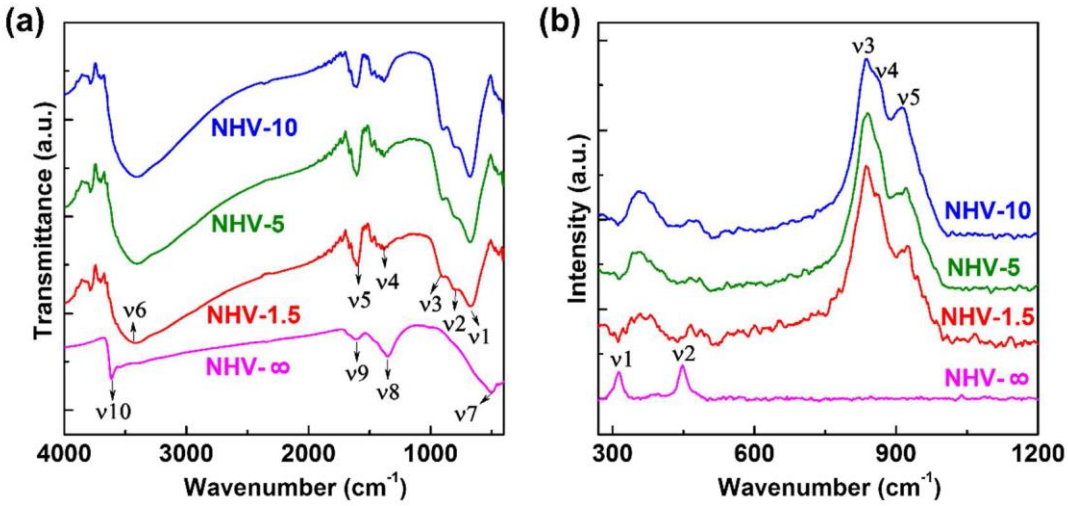

Fig. 5. Chemical bonding analysis of the nanohybrids. (a) Fourier transform infrared (FTIR) spectra and (b) μ-Raman spectra of the nanohybrids: NHV-1.5, NHV-5, NHV-10, and NHV-∞ (pristine $Ni(OH)_2$).

Fourier Transform Infrared (FTIR) and Micro-Raman Spectroscopy.

The type of intercalated POV nanoclusters and their chemical bonding natures are probed using FTIR spectroscopy. As shown in Figure 5(a), the FTIR spectrum of NHV-∞ (pristine

$Ni(OH)_2$) shows strong and sharp absorption peaks at ν9 (1604 cm^{-1}) and ν10 (3610 cm^{-1}), and these peaks are attributed to the O-H stretching and bending modes of the $Ni(OH)_2$ and free H_2O, respectively.[53] The band ν7 (500 cm^{-1}) is due to metal and oxygen bonding. Alternatively, the FTIR spectra of the NHV nanohybrids is complicated, and they show additional absorption peaks. The strong and sharp absorption peak at ν1 (670 cm^{-1}) and the shoulder band at ν2 (810 cm^{-1}) are attributed to the antisymmetric and symmetric stretching modes of the V–O–V chains, respectively.[54,55] Furthermore, the second shoulder band ν3 (910 cm^{-1}) at a higher wavenumber is assigned to the symmetric stretching mode of the terminal V=O groups.[56,57] The mild bands at ν4 and ν8 (1386 cm^{-1}) are attributed to the carbonate that is likely adsorbed on the external surface of the samples due to the high pH of the CSG.[51] The presence of these bands confirms the incorporation of the POV ions into the interlayer spaces of the $Ni(OH)_2$.

The microscopic structural properties of the samples are further examined using Raman spectroscopy, as shown in Figure 5(b). The Raman spectrum of the NHV-∞ (pristine $Ni(OH)_2$ with no POV) shows two main peaks, ν1 (313 cm^{-1}) and ν2 (448 cm^{-1}), and these peaks are attributed to the Raman-active E_g and A_{1g} mode vibrations of β-$Ni(OH)_2$, respectively.[58,59] In contrary, the NHV samples show additional vibrational modes at higher wavenumbers. The ν3, ν4, and ν5 peaks are attributed to the second-order lattice mode of α-$Ni(OH)_2$ and the symmetric stretching vibrational modes of $[V_2O_7]^{4-}$ and $[V_4O_{12}]^{4-}$, respectively.[58,60] The broad features of ν8 and ν9 from 3500 cm^{-1} to 3690 cm^{-1} are attributed to the internal O−H stretching modes from the lattice OH and the intersheet H_2O (**Supporting Fig. S4**).[53] Careful observation of the peaks clearly shows the signals shifting to lower frequencies, and which is due to the decreasing POV chain length.[61] The observed Raman features clearly reveal the intercalation of $[V_2O_7]^{4-}$ in the NHV-5 and NHV-10 nanohybrids and $[V_4O_{12}]^{4-}$ in the NHV-1.5 nanohybrid.

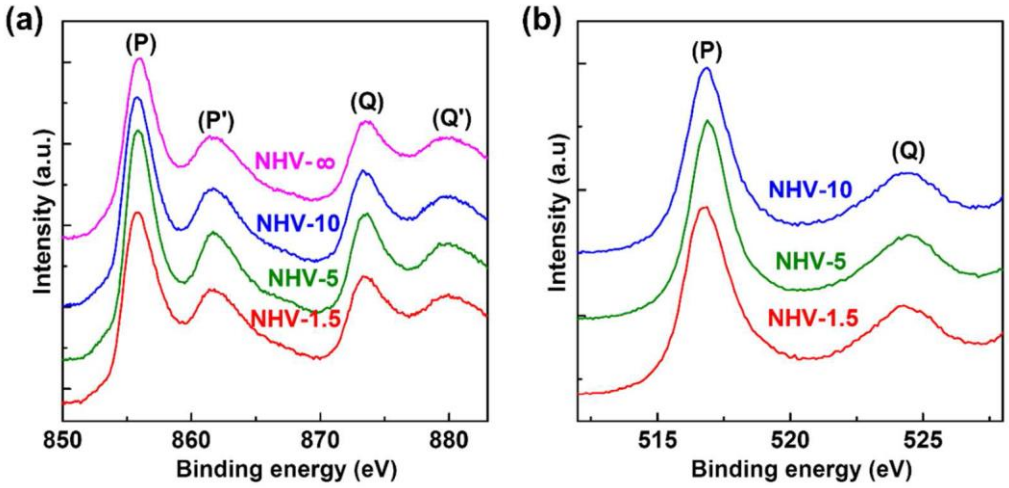

Fig. 6. Chemical states of the nanohybrids. X-ray photoelectron spectroscopy (XPS) spectra of (a) the Ni 2p and (b) V 2p core levels for the nanohybrids: (red) NHV-1.5, (green) NHV-5, (blue) NHV-10, and (pink) NHV-∞.

The various chemical states of the intercalated POV species and their effect on the chemical bonding nature of the host-$Ni(OH)_2$ lattice are investigated using X-ray photoelectron spectroscopy (XPS) measurements. Figure 6(a) shows the XPS spectra of the Ni 2p core level in the NHV nanohybrids. The Ni $2p_{3/2}$ and Ni $2p_{1/2}$ signals are clearly evident and separated by a spin-energy difference of 17.6 eV.[10,62] The characteristic satellite peaks (P′ and Q′) of each signal are also seen at the higher binding energies.[63,64] The V 2p XPS spectra of the NHV nanohybrids are illustrated in Figure 6(b). All of the NHV nanohybrids show two spectral features that arise from spin–orbit splitting, which correspond to V $2p_{3/2}$ at 517 eV andV $2p_{1/2}$ at 524 eV.[65,66] The high intensity at 517 eV is attributed to the pentavalent vanadium in the intercalated POV. The observed XPS features provide a strong evidence for the presence of Ni^{+2} and V^{+5}states in NHVs, confirming the incorporation of the POV ions into the interlayer spaces of the $Ni(OH)_2$.

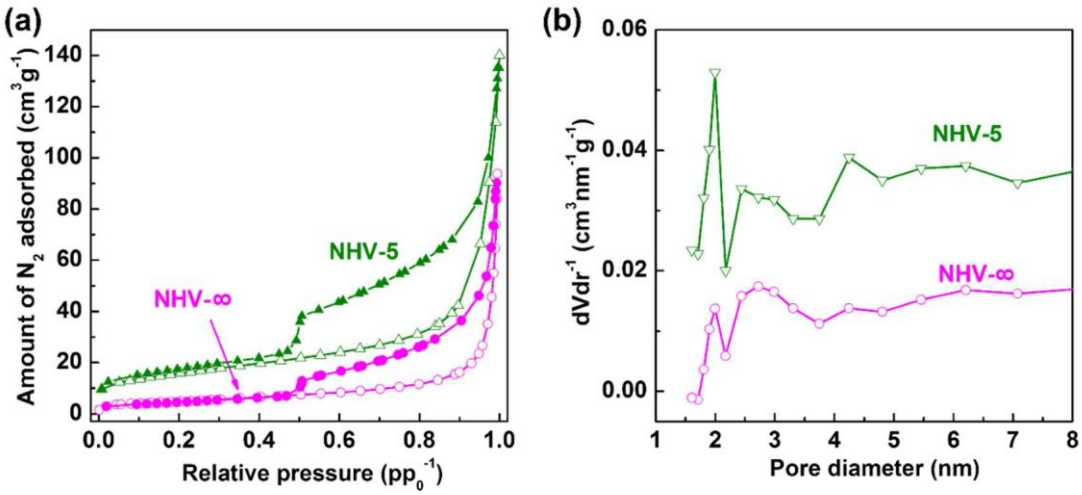

Fig. 7. Porosity analysis. (a) N_2adsorption–desorption isotherms and (b) pore size distribution curves calculated using the Barrett–Joyner–Halenda (BJH) equation for (pink) NHV-∞ (pristine $Ni(OH)_2$) and (green) NHV-5. In (a), the open and closed symbols represent the adsorption and desorption data, respectively.

N_2 Adsorption–Desorption Isotherm Analyses of the NHV nanohybrids.

The evolution of the pore structure and surface area of the NHV-5 nanohybrid and pristine $Ni(OH)_2$ are examined using N_2 adsorption–desorption isotherm measurements. As illustrated in Figure 7, the NHV nanohybrid exhibits significant N_2 adsorption in the low pressure region ($pp_0^{-1} < 0.4$) with a distinct hysteresis in the high pressure region ($pp_0^{-1} > 0.45$) correspond to that of the pristine $Ni(OH)_2$, representing the incorporation of micropores and mesopores in the materials.[37-40] The isotherms with hysteresis behavior are classified as Brunauer–Deming–Deming–Teller (BDDT)-type IV shapes and H2-type hysteresis loops based on the IUPAC classification.[67] The presence of the type IV isotherm with H2 hysteresis is

characteristic of a mesoporous material with a high adsorption energy and well-ordered, interconnected pores with narrow and wide sections.[68] The combination of the type IV isotherm and H2-type hysteresis indicates the presence of open, slit-shaped capillaries with very wide bodies (formed by parallel walls) and short, narrow necks, which is frequently observed for aggregates of plate-like particles with slit-shaped pores.[69] The surface areas of the NHV nanohybrids and pristine $Ni(OH)_2$ are calculated using the Brunauer–Emmett–Teller (BET) equation. The NHV-5 nanohybrid demonstrates an expanded surface area of 55 m^2g^{-1}, which is much larger than that of the pristine $Ni(OH)_2$ (17 m^2g^{-1}). This result underscores the effectiveness of POV-assisted intercalative hybridization via the CSG method for expanding the surface area of the layered hydroxide material. The pore size distribution is calculated according to the BJH method. Both the pristine and hybridized samples show mesopores with an average diameter of >2-5 nm, indicating the mesopores in both samples originate from the growth of the house-of-cards-type morphology in the CSG. Along with the mesoporous character, the NHV nanohybrid also exhibits a maximum distribution of pores with an average diameter of ~1.7 nm, highlighting the existence of micropores that originate from the intercalative structure. This result clearly demonstrates the advantage of the CSG method for optimizing the pore structure of the resulting intercalative NHV nanohybrid.

Oxygen evolution reaction electrocatalysis.

The effects of the POV intercalation on the OER catalytic activity of the host $Ni(OH)_2$ nanosheets are examined using linear sweep voltammetry (LSV), chronopotentiometry, and impedance analyses. The electrochemical characteristics of the NHV-nanohybrid OER catalysts are investigated using a standard three-electrode electrochemical cell, and the 1cm × 1cm NHV

nanohybrid thin films, platinum mesh, and a saturated calomel electrode (SCE) serve as the working, counter, and reference electrodes, respectively. The LSV curves of the NHV-nanohybrid electrodes were measured in a 1 M potassium hydroxide (KOH) electrolyte with a scan rate of 10 mVs^{-1}. The overpotential η values are calculated according to the following relation,

$$\eta = E_{RHE} - 1.23, (E_{RHE} = E_{vs\ SCE} + E_{0\ SCE} + 0.059\ pH) \quad (5)$$

where E_{RHE}, $E_{vs\ SCE}$, and $E_{0\ SCE}$ are the converted potential with respect to reversible hydrogen electrode (RHE), experimentally measured potential against the SCE reference electrode, and the standard potential of the SCE reference electrode at 25 °C (0.241 V), respectively.

The significantly improved water oxidation activities of the nanohybrid materials are investigated using the onset overpotential at a current density (*J*) of 10 $mAcm^{-2}$, the Tafel slope, and the current density at a higher overpotential (300 mV). The overpotential, η, required to drive the current density of 10 $mAcm^{-2}$ is evaluated because it represents the expected current at the anode in a 10 % efficient solar water splitting device under 1 sun illumination. Figure 8 (a) shows the characteristic LSV curves of the pristine $Ni(OH)_2$ and NHV nanohybrids. The pristine $Ni(OH)_2$ electrocatalyst demonstrates a typical LSV curve with an onset overpotential of 256 mV and an overpotential of 359 mV to drive a current density of 10 $mAcm^{-2}$. The Tafel slope is 85 $mVdec^{-1}$.

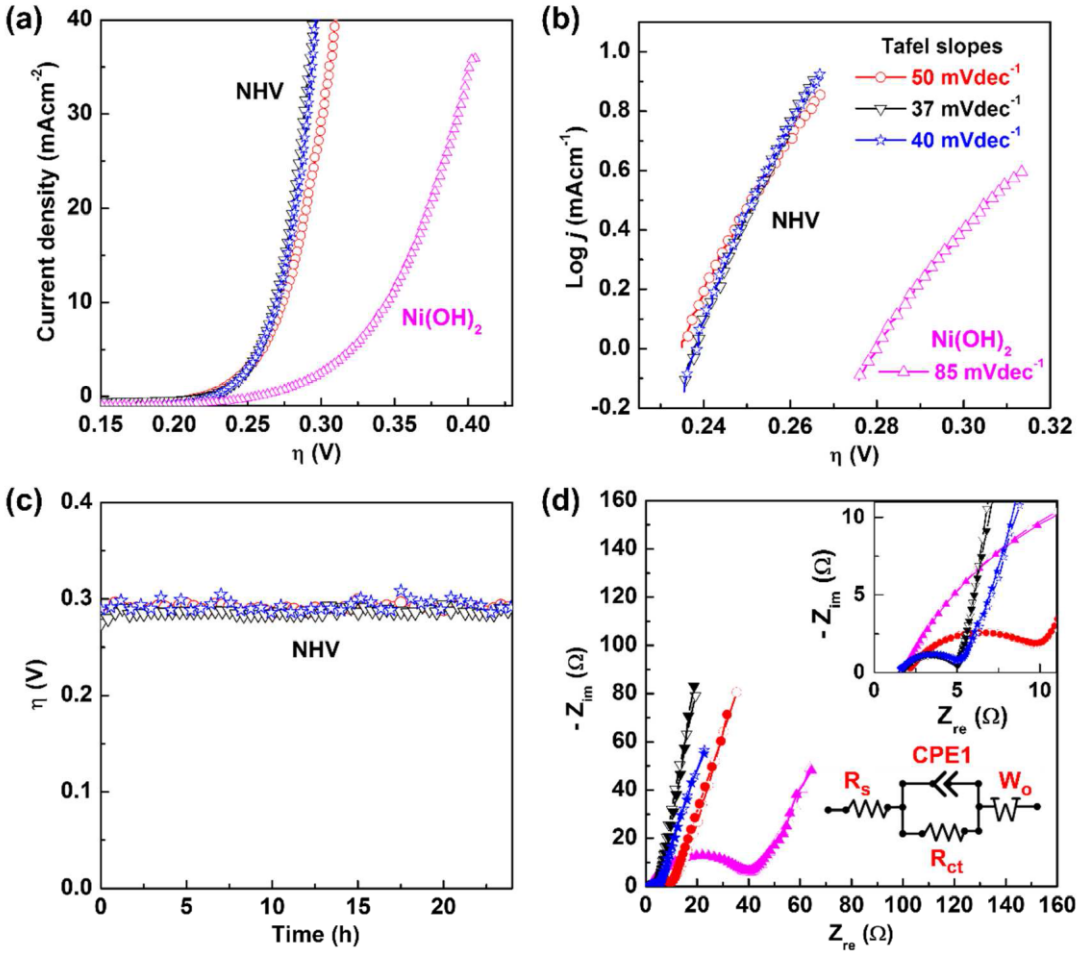

Fig. 8. OER activity and stability of the nanohybrids. (a) LSV curves at a scan rate of 10 mVs^{-1}, (b) Tafel plots, (c) chronopotentiometry curve at a constant current density of 10 $mAcm^{-2}$, and (d) Nyquist plots of the NHV nanohybrid electrodes. NHV-1.5 (circle), NHV-5 (triangle down), NHV-10 (star), and NHV-∞ (triangle up). The inset in (d) shows the enlarged view of the electrochemical impedance spectroscopy (EIS) spectra in the high frequency region with the equivalent circuit for the simulated Nyquist curves (open symbols).

Upon the intercalative hybridization with POV nanoclusters, the catalytic currents of the present nanohybrid $Ni(OH)_2$ materials considerably shift to lower potentials, which highlights the crucial role of POV intercalation in improving the electrocatalytic OER activity of the NHV nanohybrids. The onset overpotential values of the NHV-1.5, NHV-5, and NHV-10 samples are

220, 222, and 226 mV, respectively, and the overpotential values required to drive a current density of 10 $mAcm^{-2}$ are 273, 268, and 269 mV, respectively (see Figure 8(a)). The corresponding Tafel slopes of the NHV-1.5, NHV-5, and NHV-10 samples substantially improve from that of pristine $Ni(OH)_2$ (85 $mVdec^{-1}$) and are 50, 37, and 40 $mVdec^{-1}$, respectively. The observed reduction in the overpotential upon the intercalation of POV nanoclusters is attributable to the expanded interlayer-gallery height of the host $Ni(OH)_2$ nanosheet lattice, leading to an increase in the freely accessible interlayer-gallery space for the OER redox reaction electrolyte ions. Moreover, the formation of the mesoporous house-of-cards-type morphology in the $Ni(OH)_2$−POV also contributes to the increase in the surface area, leading to an increase in the number of surface catalytic sites. The expansion of the surface area is confirmed by electrochemical active surface area (ECSA) (supporting Information S7).

All of the $Ni(OH)_2$–POV nanohybrids demonstrate the redox peaks that correspond to $Ni(OH)_2$ (supporting Information S3). The quasi reversible oxidation and reduction peaks are ascribed to the oxidation of α-$Ni(OH)_2$ to α-NiOOH and the successive reduction back to α–$Ni(OH)_2$ can be observed in the CV cycles. After consecutive CV cycle, α-$Ni(OH)_2$ in $Ni(OH)_2$–POV nanohybrids is mostly converted to α-NiOOH followed by γ-NiOOH which is the key factor for the origin of electrocatalytic activity of $Ni(OH)_2$.

As shown in Figure 8(c), the long-term electrochemical stability of the NHV nanohybrids is also confirmed using chronopotentiometry for 25 h. During the stability test, all of the nanohybrids show vigorous and continuous gas evolution on the catalyst surface. Fairly constant overpotential is observed during the stability test, clearly demonstrating their highly stable OER activity. As compare to the recent reports on OER based on nickel hydroxide, carbon and noble

metal, present NHV nanohybrids demonstrated excellent OER activity (see the brief literature survey in Supporting Table S1 and S2).

The observed water oxidation activities of the NHV nanohybrids are far superior to that of the recently reported Ni-V based LDH,[10] underscoring the excellent role of POV nanoclusters as intercalating species to improve the water oxidation activity of pristine $Ni(OH)_2$ materials. Furthermore, based on the structural analysis, the NHV nanohybrids prepared with high $Ni(OH)_2$–POV ratios contain dimeric pyrovanadate $[V_2O_7]^{4-}$ ions, and the NHV nanohybrid with the lowest $Ni(OH)_2$–POV ratio of 1.5 contains more condensed, cyclic metavanadate $[V_4O_{12}]^{4-}$ ions. Furthermore, the different molecular sizes of the $[V_2O_7]^{4-}$and $[V_4O_{12}]^{4-}$POV ions also contribute to the dissimilar water oxidation activity of the NHV nanohybrids. Both types of POV ions are isovalent, but they possess different molecular sizes. The $[V_4O_{12}]^{4-}$ cyclic metavanadate ion is markedly larger than that of the dimeric pyrovanadate $[V_2O_7]^{4-}$ ion, and the unoccupied interlayer spaces in NHV-5 and NHV-10 are likely to be larger than those in the NHV-1.5 nanohybrid. The unoccupied interlayer spaces in the NHV nanohybrids cause the catalytic interlayer sites to be available for the water oxidation reaction. Since the OER primarily occurs on the surface of the NHV catalyst, the access to the unoccupied interlayer spaces in NHV-5 and NHV-10 due to the intercalation of smaller $[V_2O_7]^{4-}$ionsresults in the NHV-5 and NHV-10 nanohybrids having superior OER activity to that of NHV-1.5.

To understand the charge transport mechanisms of the observed superior electrochemical activities of the $Ni(OH)_2$–POV thin film electrodes, EIS measurements are performed in the same aqueous 1 M KOH electrolyte. Figure 8(d) shows the Nyquist plots for the NHV-nanohybrid electrodes and the simulation equivalent circuit. All of the electrodes show partially overlapping semicircles in the high-frequency region. The presence of semicircles is linked to the

electrolyte resistance (R_e) and charge transfer resistance (R_{ct}). The NHV–POV nanohybrid electrodes show smaller R_e values than the pristine $Ni(OH)_2$ electrode, indicating improvements in the charge transfer and electrical conductivity upon the POV intercalation. The NHV-nanohybrid electrode prepared with the highest $Ni(OH)_2$–POV ratio displays the smallest semicircle among the electrodes. As discussed earlier, because the surface areas of the electrode materials are comparable, the sizes of the semicircles are likely determined by the electrical conductivity of the NHV electrodes. The inclined lines in the low-frequency region correspond to the Warburg impedance that is associated with the diffusion of the electrolyte ions into the bulk electrodes. Compared with the pristine $Ni(OH)_2$ electrode (NHV-∞), the slopes of the other NHV–POV nanohybrid materials are much larger, and this implies a lower resistance for electrolyte ion diffusion through the electrode. As estimated from the simulation results, all of the NHV nanohybrids show considerably lower R_s and R_{ct} values than those of the pristine $Ni(OH)_2$. The extracted R_s and R_{ct} values are 1.76 Ω and 37.56 Ω for the NHV-∞, 2.02 Ω and 8.62 Ω for the NHV-1.5, 1.69 Ω and 3.53 Ω for the NHV-5, and 1.45 Ω and 3.98 Ω for the NHV-10. Therefore, the significant performance enhancement in the NHV–POV nanohybrid electrodes is due to the improved electrical conductivity and electrolyte ion diffusion.

Conclusions

In this study, a facile, one-step CSG method is developed to deposit intercalated structures of 2D $Ni(OH)_2$ nanosheets and 0D POV. The deposition of the ordered, intercalated architectures relies on the controlled heterogeneous precipitation of metal ions in the presence of the POV ions. Fine tuning the $Ni(OH)_2$/POV molar ratio is an effective method for selecting the type of intercalated POV species and leads to a remarkable improvement in the electrocatalytic water

oxidation activity. The best optimized NHV nanohybrid demonstrates excellent OER activities with an overpotential of 268 mV at 10 $mAcm^{-2}$ and a Tafel slope of 37 mV/decade which are considerably enhanced compared with those of the pristine $Ni(OH)_2$. The significant enhancement in the water oxidation activity of the NHV nanohybrids is attributed to the formation of a highly porous house-of-cards-type interconnected network morphology, increased freely accessible gallery space and improved electrical conductivity. The present study clearly demonstrates the effectiveness of the CSG method for the direct deposition of highly porous metal-hydroxide materials intercalated with 0D polyoxometalate for the exploration of efficient, hydroxide-based electrode materials for the OER. The present experimental findings suggest that a facile, one-step CSG deposition of NHV-nanohybrid materialsmight have numerous excellent functionalities for applications such as the production of Li-ion batteries and biosensors.

Experimental Section

Preparation of the $Ni(OH)_2$-POV nanohybrids:

The $Ni(OH)_2$–POV nanohybrid thin films were synthesized using a chemical solution growth (CSG) method. Typically, a 0.1 M aqueous solution of nickel (II) chloride ($NiCl_2$) was complexed via the addition of ammonium hydroxide (NH_4OH). The addition of NH_4OH led to an initial green-coloured precipitate of $Ni(OH)_2$, which dissolved back into the solution after the addition of excess NH_4OH. The POV anion precursor was derived from an aqueous 0.1 M sodium orthovanadate solution. The CSG bath was obtained by mixing the previously mentioned solutions into a 50 mL glass beaker with the sequential addition of a nickel amine complex and the POV anion precursor. All of the precursors were made in decarbonated water to avoid any interference from carbonate anions. The final pH of the bath was adjusted to ~13 using NH_4OH. The relative quantities of the nickel amine complex and the POV anion precursor were varied to tune the chemical composition. The stainless steel (SS) substrateswere cleaned with zero-grade polishing paper followed by washing with water. The pre-cleaned SS substrates were suspended in the solution bath parallel to the beaker wall. During the course of the CSG, the deposition assembly was covered with a lid and maintained in a water bath at 50 °C for 3 h. After the deposition, the $Ni(OH)_2$–POV nanohybrid thin films were removed from the bath, rinsed thoroughly with an ample quantity of decarbonated water, and then dried under an argon (Ar) flow. Alternatively, an attempt was made to synthesize the bulk NHV homologues from the same bath. The resulting NHV nanohybrids were separated using centrifugation, washed with water, and finally vacuum-dried at 65 °C for 24 h. All of the preparation processes in this work were performed using decarbonated water under a CO_2-free N_2 atmosphere to prevent the contamination of the LDH materials with carbonate ions.

Characterization:

The crystal structures of the $Ni(OH)_2$ and NHV nanohybrids were studied using powder XRD with Ni-filtered Cu Kα radiation and a Rigaku diffractometer. The intercalative stacking structures of $Ni(OH)_2$ and POV were probed via HR-TEM and SAED analyses using the Jeol(3000F) microscope at an accelerating voltage of 300 kV with a camera length of 255.8 mm. The hybrid structures of the nanohybrids were also probed using scanning transmission electron microscopy-bright field (STEM-BF) and scanning transmission electron microscopy-high angle annular dark field (STEM-HAADF) analyses (Jeol 2100). The surface area and pore structure of the nanohybrids were examined by volumetrically measuring the N_2 adsorption–desorption isotherms at a liquid nitrogen temperature using the Micromeritics ASAP 2020 instrument (Micromeritics, U.S.A). The samples were degassed at 90 °C for 12 h under a vacuum before the adsorption measurements. Micro-Raman and FTIR spectroscopic analyses were performed to study the chemical bonding nature of the pillared species in the present nanohybrids. The FTIR spectra in the frequency range of 400–4000 cm^{-1}were recorded using a Jasco FT/IR-6100 FT spectrometer (Jasco, Germany). The micro-Raman spectra were collected using a JY Lab Ram HR spectrometer (Horiba, Japan) with an Ar laser and a wavelength of 514.5 nm as the excitation source. The XPS data were recorded using a PHI 5100 spectrometer (Perkin Elmer, U.S.A). For the XPS spectrometer, a twin X-ray beam source was adopted, leading to wide spreading of the X-ray beam and minimization of the charging effect.

Electrochemical Measurements:

The electrocatalytic OER activity of the NHV-nanosheet thin films was investigated using cyclic voltammetry (CV), LSV, and EIS. The electrochemical measurements were performed using a standard three-electrode electrochemical cell with the Versa-stat-3 electrochemical workstation (Princeton Applied Research, U.S.A.). The NHV-nanosheet thin films with a precisely deposited unit area, a SCE, and platinum mesh served as the working, reference, and counter electrodes, respectively, and an aqueous 1 M KOH solution was used as the electrolyte. The NHV-nanohybrid electrodes were electrochemically pre-conditioned prior to each electrochemical experiment using 100 CV cycles between 0 to 0.6 V vs SCE at a scan rate of 10 mAs^{-1} in 1 M KOH to achieve stable current values. The long term stability of the NHV nanohybrid electrodes were probed using chronopotentiometry (CP) with an identical electrochemical cell as stated above with the Hg/HgO reference electrode.

Acknowledgements

The authors would like to thank the financial support from the National Research Foundation (NRF) of Korea (Grant nos. 2018R1A2B6007436, 2016R1A6A1A03012877, 2015R1D1A1A01058851 and 2018R1D1A1B07049046).

Appendix A. Supporting information

Supplementary data associated with this article can be found in the online version at

References

1. N. S. Lewis, D. G. Nocera,*Proc. Natl Acad. Sci. U S A* **103** (2006) 15729-15735.
2. M. G. Walter, E. L. Warren, J. R. McKone, S. W. Boettcher, Q. Mi, E. A. Santori, N S. Lewis,*Chem. Rev.* **110** (2010) 6446-6473.
3. Y.Liang, Y.Li, H.Wang, H. Dai, *J. Am. Chem. Soc.* **135** (2013) 2013-2036.
4. H. B. Gray, *Nat. Chem.* **1** (2009) 7.
5. M. Carmo, D. L. Fritz, J. Merge, D. A. Stolten, *Int. J. Hydrogen Energ.* **38** (2013) 4901-4934.
6. N.T. Suen, S.F. Hung, Q. Quan, N. Zhang, Y.J. Xu, H. M. Chen, *Chem. Soc. Rev.* **46** (2017) 337-365.
7. I. Roger, M. A. Shipman, M. D. Symes, *Nat. Rev. Chem.* **1** (2017) 0003.
8. Y. Jiao, Y. Zheng, M. Jaroniec, S. Z.Qiao, *Chem. Soc. Rev.* **44** (2015) 2060-2086.
9. Z. L. Wang, D. Xu, J. J. Xu, X. B. Zhang,*Chem. Soc. Rev.* **43** (2014) 7746-7786.
10. K. Fan, H. Chen, Y. Ji, H. Huang, P. M. Claesson, Q. Daniel, B. Philippe, H. Rensmo, F. Li, Y. Luo, L. Sun, *Nat. Commun.* **7** (2016) 11981.
11. L.Chen, X. Dong, Y. Wang,Y.Xia, *Nat. Commun.* **7** (2016) 11741.
12. F. Song, X. Hu, *Nat. Commun.* **5** (2014) 4477.
13. M. Gao, W. Sheng, Z. Zhuang, Q. Fang, S. Gu, J. Jiang, Y. Yan,. *J. Am. Chem. Soc.* **136** (2014) 7077-7084.
14. Y. Li, M. Gong, Y. Liang, J. Feng, J. E. Kim, H. Wang, G. Hong, B. Zhang, H. Dai, *Nat. Commun.* **4** (2013) 1805.
15. M. Gong, Y. Li, H. Wang, Y. Liang, J. Z. Wu, J. Zhou, J. Wang, T. Regier, F. Wei, H. Dai, *J. Am. Chem. Soc.* **135** (2013) 8452-8455.
16. Z. Xing, L. Gan, J. Wang, X. Yang, *J. Mater. Chem. A* **5** (2017) 7744-7748.
17. Y. Rao, Y. Wang, H. Ning, P. Li, M. Wu, *ACS Appl. Mater. Interfaces* **8** (2016) 33601-33607.
18. S., Anantharaj, P. E. Karthik, S. Kundu, *Catal. Sci. Technol*. **7** (2017) 882-893.
19. L. A. Stern, X. Hu, *Faraday Discuss.* **176** (2014) 363–379.
20. F. Song, X. Hu, *J. Am. Chem. Soc.* **136** (2014) 6481–16484.

21. Q. Zhang, C. Zhang, J. Liang, P. Yin, Y. Tian, *ACS Sustainable Chem. Eng*. **5** (2017) 3808−3818.

22. A. C. Thenuwara, N. H. Attanayake, J. Yu, J. P. Perdew, E. J. Elzinga, Q. Yan, D. R. Strongin, *J. Phys. Chem. B* **122** (2018) 847–854.

23. M. Ma, R. Ge, X. Ji, X. Ren, Z. Liu, A. M. Asiri, X. *ACS Sustainable Chem. Eng*. **5** (2017) 9625–9629.

24. R. M. Yadav, J. Wu, R. Kochandra, L. Ma, C. S. Tiwary, L. Ge, G. Ye, R. Vajtai, J. Lou, P. M. Ajayan, *ACS Appl. Mater. Interfaces* **7** (2015) 11991–12000.

25. X. Qiao, S. Liao, R. Zheng, Y. Deng, H. Song, L. Du, *ACS Sustainable Chem. Eng*. **4** (2016) 4131–4136.

26. T. Y. Ma, J. Ran, S. Dai, M. Jaroniec, and S. Z. Qiao, *Angew. Chem. Int. Ed*. **54** (2015) 4646-4650.

27. D. He, Y. Xiong, J. Yang, X. Chen, Z. Deng, M. Pan, Y. Li, S. Mu, *J. Mater. Chem*. A **5** (2017) 1930-1934.

28. P. Chen, T. Zhou, L. Xing, K. Xu, Y. Tong, H. Xie, L. Zhang, W Yan, W Chu, C Wu, Y Xie, *Angew. Chem. Int. Ed.* **56** (2016) 610-614.

29. X. Lu, W. L. Yim, B. H.R. Suryanto, C. Zhao, *J. Am. Chem. Soc.* **137** (2015) 2901–2907.

30. Y. Zhao, K. Kamiya, K. Hashimoto, S. Nakanishi, *J. Phys. Chem. C* **119** (2015) 2583–2588.

31. A. M. El-Sawy, I. M. Mosa, D. Su, C. J. Guild, S. Khalid, R. Joesten, J. F. Rusling, and S. L. Suib, *Adv. Energy Mater.* **6** (2016) 1501966.

32. X. Yu, M. Zhang, J. Chen, Y. Li, G. Shi, *Adv. Energy Mater.* **6** (2016) 1501492.

33. R. Li, Z. Wei, X. Gou, *ACS Catal.* **5** (2015), 4133–4142.

34. C. Zhang, B. Wang, X. Shen, J. Liu, X. Kong, S. S.C. Chuang, D. Yang, A. Dong, Z. Peng, *Nano Energy* **30** (2016) 503-510.

35. X. Li, Y. Fang, S. Zhao, J. Wu, F. Li, M. Tian, X. Long, J. Jin, J. Ma, *J. Mater. Chem. A* **4** (2016) 13133-13141.

36. P. V. Kamath, G. H. A. Therese, J.Gopalakrishnan. *J. Solid State Chem.* **128** (1997) 38-41.

37. J. L. Gunjakar, T. W. Kim, I. Y. Kim, J. M. Lee, S. J. Hwang, *Sci. Rep.* **3** (2013) 2080.

38. S. K. Yun, T. J. Pinnavaia, *Inorg. Chem.* **35** (1996) 6853-6860.

39. M. R. Weir, R. A. Kydd, *Inorg. Chem.***37**(1998) 5619-5624.

40. J. L. Gunjakar, I. Y. Kim, S. J. Hwang, *Eur. J. Inorg. Chem.* (2015) 1198-1202.

41. D. S. Hall, D. J. Lockwood, C. Bock, B. R. MacDougall, *P. Roy. Soc. A*471:20140792.

42. G. Hodes, *Chemical solution deposition of semiconductor films*. Marcel Dekker, New York, 2003; p. 2.

43. C. F. Baes, R. E. Mesmer, In *The hydrolysis of cations*. Wiley, New York,1976; p. 241.

44. Y. G. Li, B. Tan, Y. Wu, *Chem. Mater.* **20** (2008) 567-576.

45. I. Ichinose, K. Kurashima, T. Kunitake, *J. Am. Chem. Soc.* **126** (2004) 7162-7163.

46. J. Livage, *Coordin. Chem. Rev.* **178** (1998) 999-1018.

47. Y. Hayashi, *Coordin. Chem. Rev.* **255** (2011) 2270-2280.

48. B. Hou, D. Parker, G. P. Kissling, J. A. Jones, D. Cherns, D. J. Fermín, *J. Phys. Chem. C* **117** (2013) 6814-6820.

49. L.A. Stern,X.Hu, *Faraday Discuss*. **176** (2014) 363-379.

50. B. Hou, D. B. Alifonso, R. Webster, D. Cherns,M. Carmen, M. C. Galan,D. J. Fermin,*J. Mater. Chem. A*, **2** (2014) 6879-6886.

51. J. L. Gunjakar, T. W. Kim, H. N. Kim, I. Y. Kim, S. J. Hwang, *J. Am. Chem. Soc.* **133** (2011) 14998-15007.

52. C. D. Lokhande, A. M. More, J. L. Gunjakar, *J. Alloy. Compd.* **486** (2009) 570-580.

53. R. A. Nyquist, R. O. Kagel, *Infrared spectra of inorganic compounds (3800-450 cm^{-1})*. Academic Press Inc. New York,1971, p. 3.

54. F.Kooli, W.Jones, *Inorg. Chem.* **34** (1995) 6237-6238.

55. C. Barriga, W. Jones, P. Malet, V. Rives, M. A. Ulibarri, *Inorg. Chem.* **37** (1998) 1812-1820.

56. F. Kooli, W. Jones, V. Rives, M. A. Ulibarri, *J. Mater. Sci. Lett.* **16** (1997) 27-29.

57. J. L. Gunjakar, A. M. More, K.V. Gurav,C. D. Lokhande, *Appl. Surf. Sci.* **254** (2008) 5844-5848.

58. D. S. Hall, D. J. Lockwood, S.Poirier, C.Bock, B. R. MacDougall, *J. Phys. Chem. A* **116** (2012) 6771-6784.

59. D. S. Hall, D. J. Lockwood, S. Poirier, C. Bock, B. R. MacDougall, *ACS Appl. Mater. Interfaces* **6** (2014) 3141-3149.

60. M. Aureliano, C. A. Ohlin, M. O. Vieira, M. P. M. Marques, W. H. Casey, L. A. E. B. Carvalho, *Dalton Trans.* **45** (2016) 7391-7399.

61. R. L. Frost, K. L. Erickson, M. L. Weier, O. Carmody, *Spectrochim. Acta. A Mol. Biomol. Spectrosc.* **61** (2005) 829-834.

62. H. B. Li, *et al. Nat. Commun.* **4** (2013) 1894.

63. J. Yan, *et al. Adv. Funct. Mater.* **22** (2012) 2632-2641.

64. J. W. Lee, T. Ahn, D. Soundararajan, J. M. Ko, J. D. Kim, *Chem. Commun.* **47** (2011) 6305-6307.

65. S. J. Wu, X. H. Yang, J. F. Hu, H. W. Ma, Z. G. Lin, C. W. Hu, *Cryst Eng Comm* **17** (2015) 1625-1630.

66. G. Silversmit, D. Depla, H. Poelman, G. B. Marin, R. D. *J. Electron. Spectrosc. Relat. Phenom.* **135** (2004)167-175.

67. J. B. Condon, InSurface Area and Porosity Determinations by Physisorption: Measurements and Theory. 1st ed.; Elsevier: Amsterdam; Boston, 2006; p. 274.

68. T. Allen, InPowder Sampling and Particle Size Determination. 1st ed.; Elsevier: Amsterdam; Boston, 2003; p. 660.

69. S. J. Gregg, K. S. W. Sing, InAdsorption, Surface Area, and Porosity. 2nd ed.; Academic Press: London; New York, 1982; p. 303.

Supporting Information for

"Nanoporous Nanohybrids of Two-dimensional Layered Nickel Hydroxide Pillared with Zero-dimensional Polyoxomatalate Nanoclusters for Enhanced Water Oxidation Catalysis"

Jayavant L. Gunjakar, Bo Hou, Akbar I. Inamdar, SeungNam Cha, S. M. Pawar, Abu Talha Aqueel Ahmed, Harish S. Chavan, Jongmin Kim, Sangeun Cho, Yongcheol Jo, Seong-Ju Hwang, Hyungsang Kim and Hyunsik Im

Table S1: Survey of OER activity of $Ni(OH)_2$ based electrocatalyst.

Catalyst	Current Density	Overpotential	Tafel Slope mV/dec	Stability test	Ref.
POV intercalated-$Ni(OH)_2$	10 mV/cm^2	268 mV	37	24 hr	Present
Nanoporous nickel hydroxide@nickel ($Ni(OH)_2$@Ni) film on carbon cloth	10 mV/cm^2	458 mV	168	20 hr	1
Nanostructured α-Nickel-Hydroxide	10 mV/cm^2	331 mV	42	24 hr	2
Hydrotalcite-like $Ni(OH)_2$ Nanosheets on Ni foam	10 mV/cm^2	330 mV	150	24 hr	3
Petal-Like Hierarchical Array of Ultrathin $Ni(OH)_2$ Nanosheets Decorated with $Ni(OH)_2$ Nanoburls	10 mV/cm^2	300 mV	43	26 hr	4
Nickel–vanadium monolayer double hydroxide	10 mV/cm^2	300	50	25 hr	5
Nickel hydroxide nanoparticles	10 mV/cm^2	299	53	15 hr	6
CoMn-LDH	10 mV/cm^2	293 mV	43	14 hr	7
Orthorhombic α-NiOOH Nanosheet	10 mV/cm^2	266 mV	76.3	24 hr	8
Cobalt intercalated NiFe LDH	10 mV/cm^2	265	47	24 hr	9
Benzoate-$Ni(OH)_2$/NF	60 mV/cm2	242 mV	97	27 hr	10

Table S2: Survey of OER activity of carbon based electrocatalyst.

Catalyst	Current Density	Overpotential	Tafel Slope mV/dec	Stability test	Ref.
POV intercalated-$Ni(OH)_2$	10 mV/cm^2	268 mV	37	24 hr	Present
Carbon Nitrogen Nanotubes	10 mV/cm^2	450	330		11
Cobalt and Nitrogen Codoped Graphene with Inserted Carbon Nanospheres	10 mV/cm^2	426	69	200 lsv cycles	12
Phosphorus-Doped Graphitic Carbon Nitrides	10 mV/cm^2	400	61.6	30	13
Nanocarbon-intercalated and Fe-N-codoped graphene	10 mV/cm^2	390	96	100 cycles	14
Atomic dispersed Fe-Nx species on N and S co-decorated hierarchical carbon	10 mV/cm^2	370	82	10 000 cycles	15
Surface-Oxidized Multiwall Carbon Nanotubes	10 mV/cm^2	360	42	166 hr	16
Transition-metal-doped carbon/nitrogen (M/C/N) materials	10 mV/cm^2	360		50 cycles	17
Sulfur-Doped Carbon Nanotube–Graphene Nanolobes	10 mV/cm^2	350	95	75 hr	18
Nitrogen and Sulfur Codoped Graphite Foam	10 mV/cm^2	346	78	60	19
Nitrogen and Phosphorus Dual-doped Graphene/Carbon Nanosheets	10 mV/cm^2	340	70	16000s	20
Nitrogen-doped Ordered Mesoporous Carbon/Graphene	10 mV/cm^2	324	67	1.6 hr	21
Nitrogen-Doped Mesoporous Carbon Nanosheet/Carbon Nanotube Hybrids	10 mV/cm^2	320	55	16 hr	22

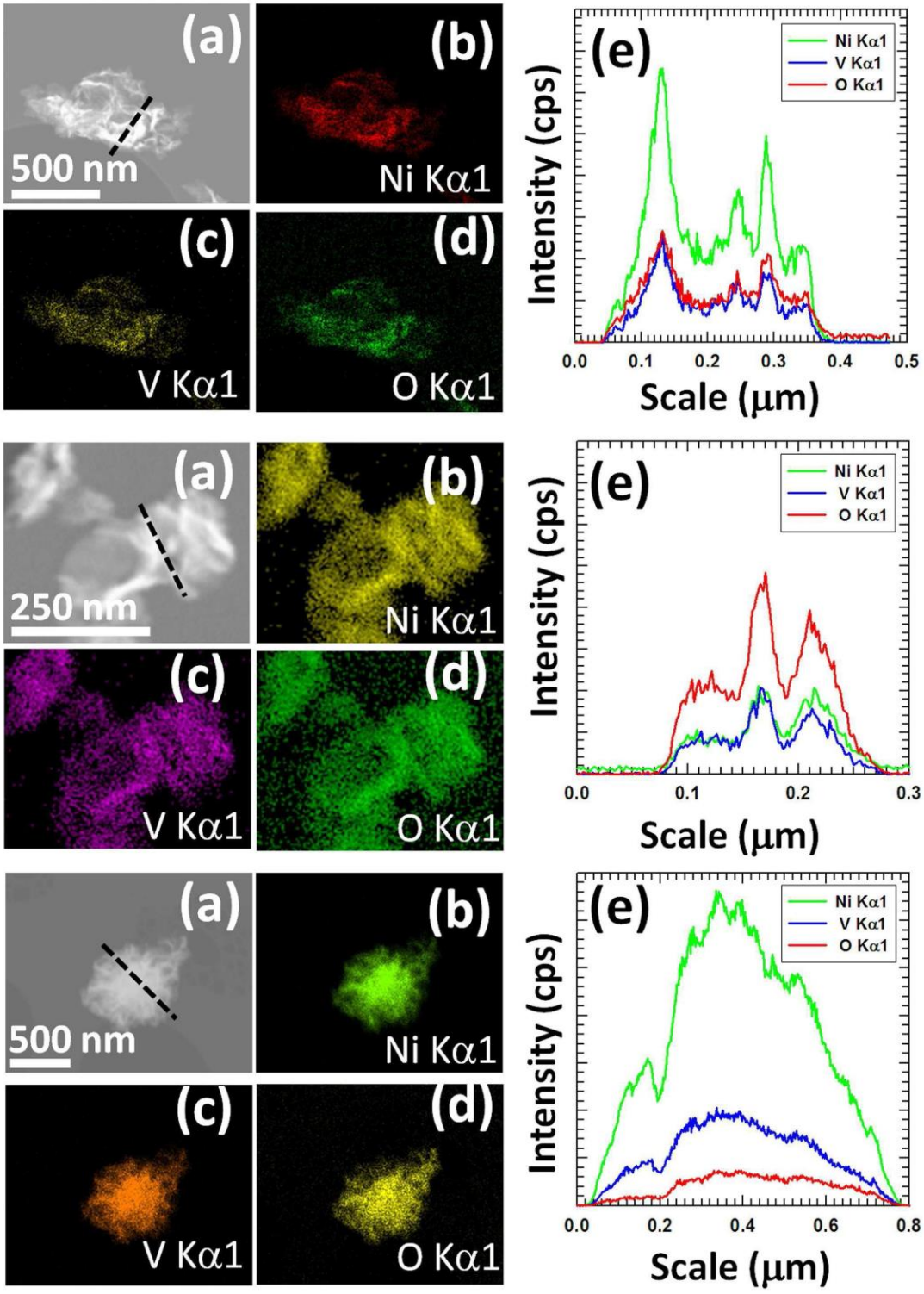

Figure S1. (a) HAADF STEM images, (b) HAADF STEM element mapping for (b) Ni, (c) V, and (e) O and (e) element line scans along the dotted line of (top) NHV-1.5, (middle) LNHV-5, (bottom) LNHV-10 nanohybrids

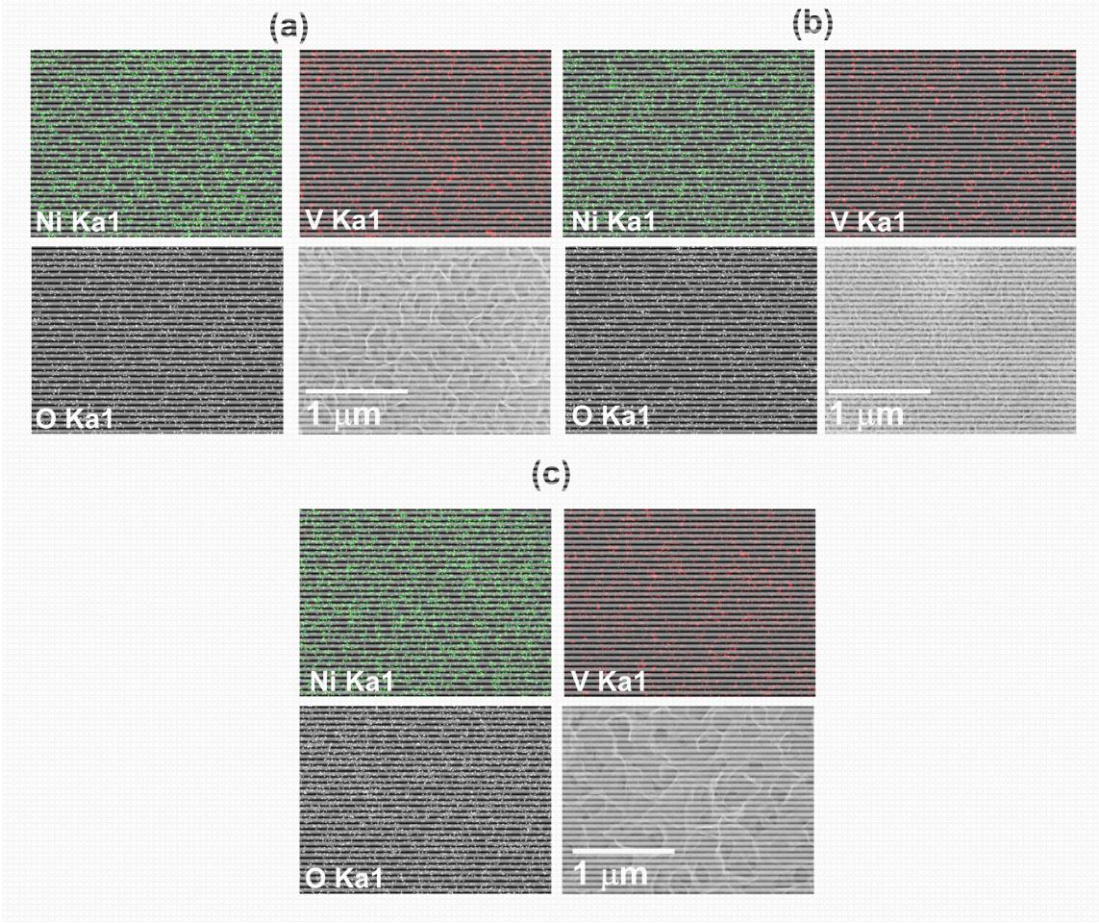

Figure S2. EDS elemental maps and FESEM micrographs of (a) NHV-1.5, (b) LNHV-5, (c) LNHV-10, and (d) LNHV-0 nanohybrids deposited on stainless steel.

The chemical compositions of the $Ni(OH)_2$–POV nanohybrids are quantitatively determined with EDS elemental mapping analyses. The EDS analysis clearly showed the homogeneous distribution of Ni, V, and O over the $Ni(OH)_2$–POV nanohybrid crystallites. Based on the EDS elemental analysis the chemical compositions of the $Ni(OH)_2$–POV nanohybrids are determined to be $Ni(OH)_{1.67}{\cdot}0.08(V_4O_{12})^{4-}{\cdot}yH_2O$, $Ni(OH)_{1.96}{\cdot}0.16(V_2O_7)^{4-}{\cdot}yH_2O$ and $Ni(OH)_{1.962}{\cdot}0.15(V_2O_7)^{4-}{\cdot}yH_2O$ for NHV-1.5, LNHV-5, and LNHV-10, respectively.

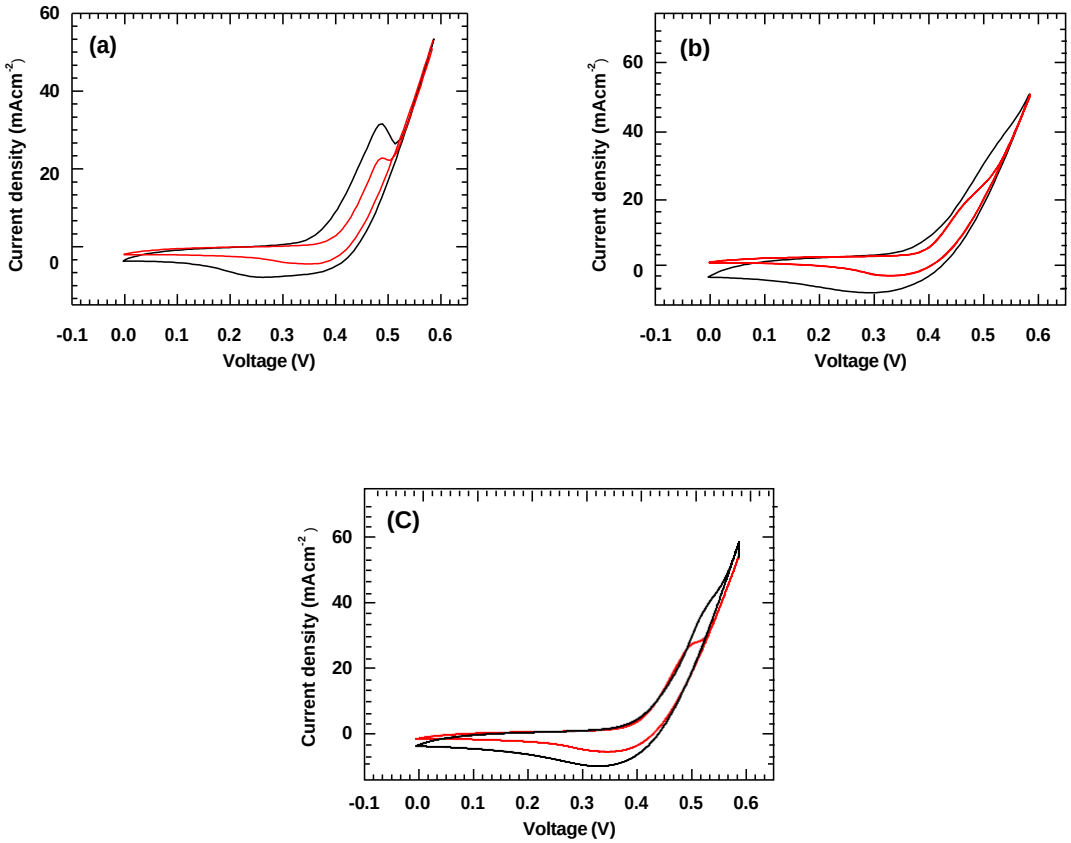

Figure S3. CV curves of (a) NHV-1.5, NHV-5 and NHV-10 nanohybrids befor stbilization (Red) and after stabilization (black) at a scan rate of 100 mVs^{-1}.